LiDARSpectra: Synthetic Indoor Spectral Mapping with Low-cost LiDARs

Jiawei Hu
University of New South Wales
CSIRO
Australia
jiawei.hu@unsw.edu.au

Yanxiang Wang
University of New South Wales
CSIRO
Australia
yanxiang.wang@unsw.edu.au

Hong Jia
University of Melbourne
Australia
hong.jia@unimelb.edu.au

Cheng Jiang
University of New South Wales
Australia
cheng.jiang1@student.unsw.edu.au

Mahbub Hassan
University of New South Wales
Australia
mahbub.hassan@unsw.edu.au

Brano Kusy
CSIRO
Australia
brano.kusy@data61.csiro.au

Wen Hu
University of New South Wales
Australia
wen.hu@unsw.edu.au
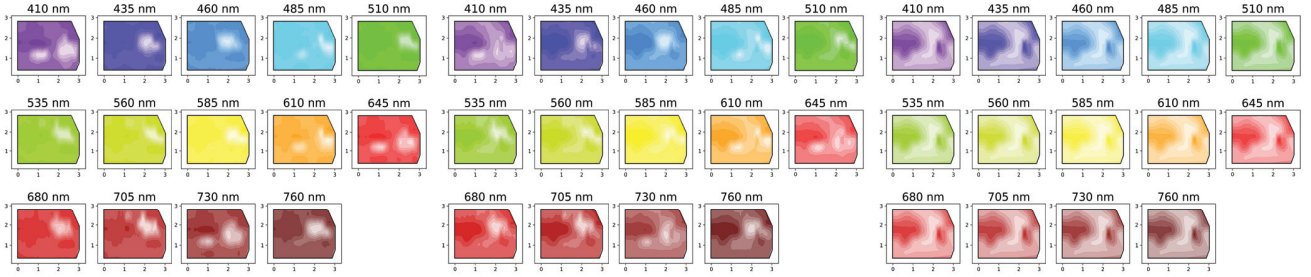
(a) Groundtruth spectra map.

(b) Synthetic spectral map produced by *LiDARSpectra*.
NRMSE = 0.283, MAPE = 12.64%.

(c) Synthetic spectral map produced by *LiDARSpectra* without Material Estimation.
NRMSE = 0.537, MAPE = 45.2%.

Figure 1: Sample spectral maps with 14 wavelengths: groudtruth vs. *LiDARSpectra* with and without material estimation. NRMSE: Normalized Root Mean Squared Error. MAPE: Mean Absolute Percentage Error.

ABSTRACT

We introduce *LiDARSpectra*, a novel approach utilizing mobile-integrated commodity Light Detection and Ranging (LiDAR) signals for synthetic indoor light spectral mapping. Our method incorporates an innovative material estimation algorithm into the LiDAR signal processing pipeline, accurately simulating reflected wavelengths from indoor surfaces. Utilizing low-resolution LiDAR scans enriched with material information, it eliminates the need for deploying dedicated spectral sensors, greatly simplifying the spectral mapping process. We validate our synthetic spectral maps against real sensor data and demonstrate their utility in applications such as indoor localization and solar energy provisioning. This presents an efficient solution for indoor spectral mapping with wide-ranging potential across fields like lighting design, indoor planting, environmental monitoring, and location-based services.

1 INTRODUCTION

Numerous applications, such as interior design [7], indoor planting [21], and human comfort management [16], necessitate access to Light Spectral Information (LSI), which refers to the varying light intensity at different wavelengths within indoor spaces. However, capturing precise LSI is challenging due to spatial variations caused by attenuation, occlusions, reflections, and temporal changes from environmental adjustments or natural light dynamics. This highlights the pressing need for a low cost and efficient solution to produce dynamic spectral maps, directly impacting fields ranging from smart building design to precision agriculture and personalized comfort systems.

Generating detailed LSI map is labor-intensive and can be approximated through a network of Internet of Things (IoT) spectral sensors or photodetectors. Integration of LSI sensors with smart building systems is an exciting new technology that can provide innovative lighting solutions [13, 23, 25]. Such systems are capable of emulating natural light cycles, promoting well-being, and improving energy efficiency by tailoring. Additionally, LSI sensor networks have potential in high-accuracy indoor localization of occupants [17, 43], supporting security and personalized environment controls.

A comprehensive spectral map is essential for the successful integration of LSI IoT systems. Such a map not only aids in selecting the optimal locations for sensor installation within buildings but can also help fine-tune the LSI user localization algorithms.

In this paper, we leverage the ubiquitous LiDAR sensors on commodity mobile phones and ray tracing algorithms to create accurate spectral maps of indoor spaces. The core concept is to harness LiDAR's ability to create a 3D model of the environment and then employ ray tracing to determine LSI at specific points of interest. As demonstrated later in this paper, this approach enables the generation of precise spectral maps within minutes using mobile phones fitted with LiDAR.

While the concept of creating a spectral map through ray tracing in a 3D LiDAR model is valid, it requires reflectance spectrum information for every surface within the LiDAR model. This data is essential for accurate tracing of reflections across the entire light spectrum, as the reflectance of a material's surface can vary with wavelength. This wavelength-dependent property is known as the material's reflectance spectrum.

Unfortunately, LiDAR systems generate 3D mesh surfaces without providing the reflectance spectrum data. The key contribution of this paper is *LiDARSpectra* - the complete signal processing pipeline that generates the reflectance spectrum data for LiDAR mesh surfaces, implements full-spectrum ray tracing, and generates precise spectral maps for indoor environments (see Figure 1).

The contributions in this paper can be summarised as follows:

- We introduce *LiDARSpectra*, an innovative LiDAR-driven approach for spectral map generation that eliminates the need for manual labour-intensive collection of spectral data in indoor spaces. To the best of the authors' knowledge, this represents the pioneering effort of its kind.
- We present a method that calculates the reflectance spectrum for each surface within the 3D LiDAR output, a crucial step in ensuring accurate ray tracing of reflections throughout the entire light spectrum.
- We deploy *LiDARSpectra* in real world experiments and produce spectral maps for an indoor space using a mobile phone. Our results show that the average error between the *LiDARSpectra*-generated spectral map and the ground truth values measured by LSI sensor network is 12%.
- We showcase the versatility of *LiDARSpectra* in two applications. First, we evaluate its efficacy in the context of LSI-based indoor localization, where location fingerprints are derived from the spectral map. Our findings reveal that utilizing *LiDARSpectra* significantly reduces localization errors in comparison to relying on fingerprints generated from outdated sensor data. This highlights the benefits of *LiDARSpectra*, capable of producing current fingerprints within minutes, in contrast to the hours needed when using sensor data. Second, we illustrate that *LiDARSpectra* can accurately generate energy harvesting maps for indoor solar cells.

The remainder of the paper is organized as follows. The system architecture of *LiDARSpectra* is detailed in Section 2. We delve into the implementation of *LiDARSpectra* and evaluate its performance in generating precise spectral maps in Section 3. We discuss the
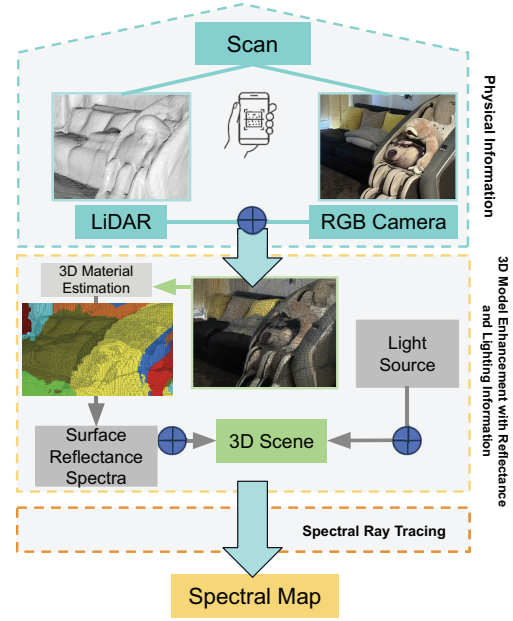

Figure 2: The system overview for *LiDARSpectra*.

limitations of our current *LiDARSpectra* prototype and provide an overview of related work in Sections 4 and 5, respectively. Finally, we conclude in Section 6.

2 LiDARSpectra: Synthetic Spectral Mapping

2.1 System Overview

LiDARSpectra is a framework that integrates LiDAR and RGB camera-based 3D scanning, material estimation, and radiance calculations, providing a comprehensive solution for spectral irradiance and solar-generated energy predictions in various applications. Figure 2 shows the end-to-end overview of *LiDARSpectra*, which starts with a 3D scan of the physical world using LiDAR and RGB camera sensors on a mobile phone. Our advanced 3D material estimation algorithm is then used to predict and assign material spectral reflectance to surfaces in the 3D scan. We combine the material reflectance data with the spectral signature of the light source, which can be obtained from the manufacturer's datasheet. Specifically, we use a radiance ray tracing engine to combine the reflectance and light source spectral data to calculate the spectral irradiance observed for the overall 3D scene.

2.2 LiDAR and RGB Camera-Based 3D Scanning

Fusion of LiDAR data with RGB images is a popular technique used in 3D scene scanning and modeling domain. Modern mobile devices, such as the iPhone 14 pro max used in this work, are commonly equipped with both sensors, allowing the users to capture precise depth information for each pixel in an image. The commodity phones can be thus used as powerful tools for reconstructing the geometry and appearance of indoor spaces.

The core of this technique lies in the respective strengths of LiDAR and RGB sensors. The LiDAR sensor measures the time it takes for a laser beam to reflect back from the environment, thus

determining the depth information $D(x, y)$ for a given pixel (x, y). This information is complemented by the RGB camera that provides a 3-channel color measurement for each pixel. The fusion process combines depth and color information, generating a 3D point cloud $P(x, y, z)$ [30]:

$$P(x, y, z) = (x, y, D(x, y)).$$

To create the 3D model of the indoor environment, the user is typically required to gently move the mobile device around the room, until all the areas have been scanned. The phone will simultaneously capture depth information using LiDAR and color information using the RGB camera.

2.3 Material Estimation

The primary objective of our material estimation algorithm (see Algorithm 1) is to accurately identify the materials corresponding to the surfaces of scanned 3D scenes. Here, we first extract a single-angle view from the 3D environment and use a 2D material segmentation (MS) method for images [4] to estimate materials for each pixel. We proceed with a database matching (DM) step, in which spectral reflectance information is determined for the identified materials using a comprehensive spectral reflectance database [19]. Finally, the 2D pixels are realigned with their original 3D mesh counterparts, ensuring an integration of spectral material properties within the 3D model. This algorithm proceeds iteratively through additional views in the 3D environment until accurate material reflectance data is available for majority of the 3D meshes.

Algorithm 1: Material Estimation Algorithm

Data: The 3D model ($M = \{(X, Y, Z)\}$), # of all 3d points N, camera parameters f and (c_x, c_y)

Result: Set of viewpoints (V) covering the 3D model

1 $V \leftarrow \{$initial viewpoint $v_0\}$;
2 $T \leftarrow$ completeness threshold;
3 $coverage \leftarrow \{\}$;
4 **while** $\frac{|coverage|}{N} < T$ **do**
5     $\{I_{(u,v)}\} \leftarrow$ CaptureImage(v_i) ;
6     $\{materials_{(u,v)}\} \leftarrow$ **DM**(**MS**$\{I_{(u,v)}\}$)) ;
7     $\{materials_{(X,Y,Z)}\} \leftarrow$ **RPP**($\{materials_{(u,v)}\}$) ;
8   **for** p in $\{materials_{(X,Y,Z)}\}$ **do**
9   **if** p is not in $coverage$ **then**
10   Append p to the $coverage$;
11   **if** $\frac{|coverage|}{N} \geq T$ **then**
12   **Break**
13   **Viewpoint Update(**V**)** ;

2.3.1 2D Material Segmentation We used the method introduced in [4] for the material segmentation (**MS**) and classification in a 2D image, which involves a multi-stage process.

The process commences with the training of a Convolutional Neural Network (CNN) specifically designed for material classification. This CNN is tailored to generate individual material predictions for given input patches. In our study, we have leveraged the
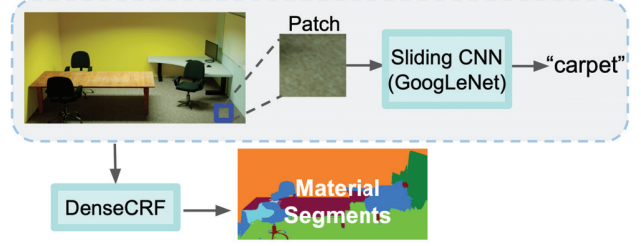

Figure 3: Material Segmentation for 2D image.

GoogLeNet [42] architecture for classification. The original model was trained using the Materials in Context Database (MINC) [4], which contains 23 material types. To better align the model with our objectives, we have removed the classes "Food," "Other," and "Pol. stone" to ensure that all classes in the model correspond to entries within the spectral reflectance database.

Subsequently, the previously trained CNN is transformed into a sliding window detector by replacing its last fully connected layers with convolutional layers. This alteration results in a fully convolutional network capable of classifying images of varying shapes and sizes, rendering it adaptable to a range of input scenarios. It is important to note that the network's weights remain fixed and unaltered following this conversion.

Using this adapted network, the process proceeds to densely classify a grid across the entirety of the image. As a consequence of the inherent strides of each layer, the network produces material predictions for every 32 pixels. To achieve finer-resolution predictions, a 16-pixel shift is introduced in the input image. This adjustment introduces minimal additional computational overhead, as the convolutional layers are efficiently reused.

Then the Conditional Random Field (CRF) method [22] has been used for coherent material segmentation and pixel-level recognition. The CRF model combines the unary term, derived from the output of the CNN network, with fully connected pairwise reasoning, taking into account spatial relationships between neighboring pixels.

2.3.2 Database Matching The material segmentation network provides material categories without color information, which is a critical attribute, particularly in the context of spectral simulation. The spectral reflectance curve of a material can vary significantly based on its color as shown in Figure 5. To bridge this gap, we introduce a database matching (**DM**) component that assigns color information to the segmented materials, and match it with a reflectance curve in the database.

For each segmented region, the RGB values of the constituent pixels are collected and as an input for our color recognition algorithm. Our goal is to account for variations in color due to lighting conditions and isolate the predominant hue. To achieve this, we firstly eliminate outliers such as highlights and shadows. The algorithm employs thresholding and statistical outlier detection techniques to flag and exclude pixel clusters that deviate significantly from the predominant hue. This ensures that the recognized color accurately represents the material's intrinsic hue, independent of external lighting effects.

After pre-filtering, we apply the K-means clustering algorithm to identify the primary colors. Here, we divide data points into K clusters, so that each cluster represents a dominant color. Let P represent the set containing all data points, and K represent the number of dominant colors. The goal of this K-means algorithm is to partition the data points in P into K clusters, where each cluster C_k has a center μ_k such that the following objective function is minimized:

$$J(C) = \sum_{k=1}^{K} \sum_{i \in C_k} |p_{(i)} - \mu_k|^2 \qquad (1)$$

where $p_{(i)}$ represents the i-th data point in the set P, C_k represents the k-th cluster, and μ_k represents the center of the k-th cluster. The objective is to choose centers μ_k and assign data points i to clusters C_k in order to minimize the overall objective function $J(C)$.

The final step involves the actual database matching to associate the primary colors with the corresponding material. For each segmented region, we find the closest color in the database and assign the segment the corresponding spectral reflectance information.

2.3.3 3D Mesh Alignment Our single-view 2D image is captured from the 3D model using perspective projection. Therefore, to align the 2D coordinates back to 3D coordinates, we employ Reverse Perspective Projection(**RPP**) [14]. This process determines the 3D world coordinates (X, Y, Z) of a point in space based on its 2D image coordinates (u, v). The core principle involves calculating the depth (Z) of the point using the focal length and the distance of the point from the principal point in the image. With the depth value known, the X and Y coordinates can be computed based on the position of the point relative to the principal point. The reverse perspective projection can be mathematically modeled as follows:

$$Z = \frac{f}{\sqrt{(u - c_x)^2 + (v - c_y)^2}} \qquad (2)$$

$$X = Z \cdot \frac{u - c_x}{f} \qquad (3)$$

$$Y = Z \cdot \frac{v - c_y}{f} \qquad (4)$$

Where (u, v) are the 2D image coordinates. (X, Y, Z) are the 3D world coordinates, f is the focal length, and (c_x, c_y) are the principal point coordinates.

Viewpoint Update. In our approach, we design a simple but effective viewpoint updating strategy for our application. Since we are primarily acquiring material information in a relatively simple room environment (which typically have a rectangular layout), we first initialize the position v_0 of the camera to the center of the room. From this center point, we systematically capture images from six different directions (i.e., east, west, north, south, up and down), thus ensuring a steady increase in material coverage. This strategy allows us to reach the desired completeness threshold T in a short period of time.

2.4 Received Light Spectral Energy

2.4.1 Spectrum of artificial light sources As shown in Figure 2, both light source and material reflectance information have significant impact on the spectral irradiance (spectral mapping). Currently,
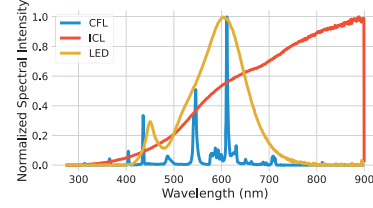

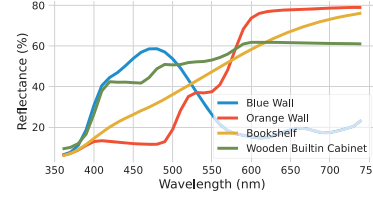**Figure 4: The SPDs of different light bulb types.**

Figure 5: The reflectance curves of different materials.

there are three main types of light bulbs in the market: incandescent light bulbs (ICL), compact fluorescent lights (CFL), and light-emitting diodes (LED). These methods generate different spectral probability densities (SPDs) as the underlying light emitting principle is quite different. Specifically, ICL produces light by heating a wire at a high temperature, covering a wide spectrum range. CFL bulbs are more complicated: they generate invisible UV light by charging a mercury vapor, which then interacts with the fluorescent coating, resulting in light emission in the visible range. LED releases light due to recombination of the injected carriers of electrons and holes which results in energy released in the form of light. The lights produced by different types of light bulbs have distinctive patterns of SPDs because of their various material structures, as shown in Figure 4. Spectrum data for different light sources is well characterized, for example, the light spectrum database [9] contains the spectrum data of 311 models of light bulbs.

2.4.2 Reflectance of objects Light generated by light sources is reflected by objects in the environment will have a different spectral signature, due to different materials, textures, and colors. Light reflectance curves for different materials can be formulated as follows:

$$R_\lambda = \frac{L_\lambda^r}{L_\lambda^i}, \qquad (5)$$

where R is the reflectance in wavelength λ, and L^r and L^i are the spectral radiance of reflected light and incident light, respectively. The reflectance varies depending on the material type and color. For instance, the orange interior wall has higher reflectance values for the red light range (622 - 780 nm) but lower ratios in the rest of the wavelength range. Reflectance of different materials can also be found in free to access external databases of materials. For example, reflectance data of 1,294 types of opaque materials were measured with a spectrometer and are available in [19]. We show the reflectance of four materials as an example in Figure 5, to illustrate the distinct reflection characteristics of these materials.

2.4.3 Spectral energy readings There are two types of lights affecting the received light energy in a surface location as follows. L_{LOS} is the light that comes directly from light sources (S), and
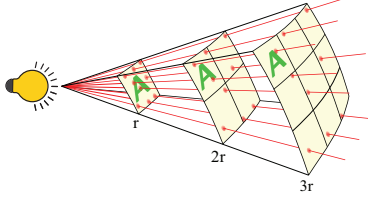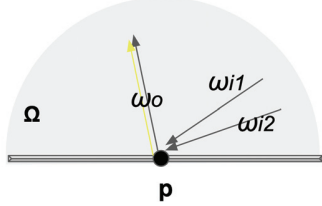
Figure 6: Inverse square law.

Figure 7: Illustration of light interaction with a surface at point p on the hemisphere.

L_{RE} is the reflected light from surrounding objects (O). Both L_{LOS} and L_{RE} follow the Inverse Square Law [36] as shown in Figure 6. Therefore, the light enters a surface location may be expressed as follows:

$$L_\lambda = L_{LOS}^\lambda + L_{RE}^\lambda$$
$$= \sum^{\forall S} \frac{L^\lambda}{a^2} + \sum^{\forall O} \frac{1}{c^2} \cdot R_\lambda (\frac{L^\lambda}{b^2}), \quad (6)$$

where L^λ is the irradiance of a light source in wavelength λ, a is the direct distance between a light source and the surface location, b is the distance between the light source and a reflective object, and c is the distance between the reflective object and the surface location. This model shows that the key parameters of of received light spectral energy readings are light source spectrum L^λ and the reflectance value R_λ, in addition to the 3D geometry of the scene. To this end, *LiDARSpectra* obtains the light source spectrum L^λ from building facility database and the reflectance value R_λ of different surfaces in the scene by the Algorithm 1, and model the interaction between light and 3D geometry of the scene with ray tracing, which will be introduced next.

2.4.4 Ray Tracing LiDARSpectra models the impact of the 3D scene geometric parameters in Eq. (6) with by making usage of a light tracing engine. Ray tracing is a fundamental technology in computer graphics and computer-generated imagery, playing a pivotal role in the generation of photorealistic images and simulations [15]. It simulates the behavior of light by tracing the paths of individual rays as they interact with surfaces in a scene. This technology enables the accurate rendering of lighting, shadows, and reflections, resulting in visually stunning and lifelike visual effects.

In the ray tracing framework, at point p, as shown in Figure 7, behavior of light can be represented as follow:

$$L_o(p, \omega_o) = L_e(p, \omega_o) + \int_\Omega f_r(p, \omega_i, \omega_o) \cdot L_i(p, \omega_i) \cdot (\omega_i \cdot n) \, d\omega_i, \quad (7)$$
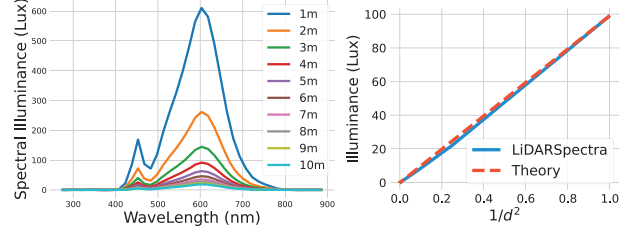

Figure 8: The impact of distance to the light energy in different spectrum (wavelengths).

where the outgoing radiance, denoted as $L_o(p, \omega_o)$, is computed as a sum of emitted radiance ($L_e(p, \omega_o)$) and the integral over the hemisphere of possible incident directions (Ω) of the product of the bidirectional reflectance distribution function (BRDF) ($f_r(p, \omega_i, \omega_o)$), the incoming radiance ($L_i(p, \omega_i)$), and the cosine term ($\omega_i \cdot n$) that accounts for the angle between the incident direction and the surface normal. The BRDF (f_r) characterizes how light is reflected from the surface, and the cosine term ($\omega_i \cdot n$) represents the geometric factor. The integration over all possible incident directions in the hemisphere (Ω) captures the contribution from all incoming light directions.

3 EVALUATION

3.1 Prototype

We implement a prototype of *LiDARSpectra*, which will be open sourced to the research community to stimulate further research.

Backend. Our prototype uses a popular ray tracing engine Radiance [44], which is also commonly used for lighting-rendering [11]. Radiance employs a hybrid method that combines deterministic ray tracing and Monte Carlo method to produce accurate and efficient results. Instead of three color channels (i.e., R, G, and B) that are commonly used, our prototype supports ray tracing process for arbitrary spectral input, i.e., wavelength power λ.

Frontend. Our prototype uses Vi-Suite [40] and Blender [6] tools to explore, manipulate, and visualize the 3D environments, including light sources, objects, and the light spectrum energy observation locations. Furthermore, the prototype support users to customize the two key parameters of light source spectrum and object reflectance (see Section 2.4.3) to produce more accurate synthetic spectral maps.

3.2 Microbenchmark

To understand the performance of *LiDARSpectra* on modeling common light behaviors, we conducted experiments in three scenarios to explore light propagation rules: (1) Inverse Square Law, (2) Light Superposition, and (3) Reflectance. **Inverse Square Law.** To verify the correctness of the Inverse Square Law [36], we create a scene where the light source is fixed to a BR30 LED light bulb. We moved the groundtruth light spectrometer away from the light source, taking a measurement every 0.1cm, one hundred measurements in total.

From Figure 8 (left), we can observe that as the distance increases, the spectrum distribution remains the same, but the light intensity decreases non-linearly. Furthermore, we plot a graph of the rate of reaction over $\frac{1}{d^2}$ as shown in Figure 8 (right). The linear relationship
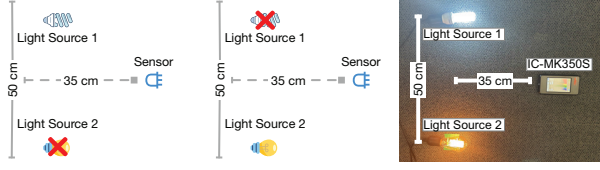
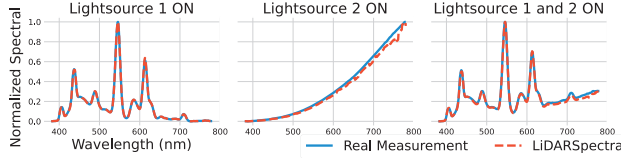Figure 9: Synthetic and real measurement setups for the superposition of lights.

Figure 10: SPDs of real and synthetic measurements with the sensor at the middle point.
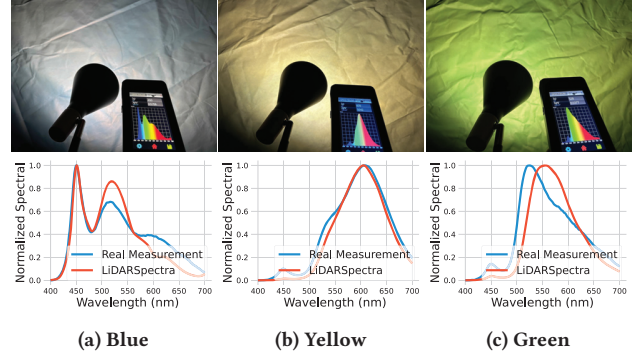

(a) Blue (b) Yellow (c) Green

Figure 11: Reflectance verification with different color fabric.

3.3 Evaluation of Synthetic Spectral Map Generation

Our goal is to show that *LiDARSpectra* produces accurate synthetic spectral maps in realistic and non-controlled indoor environments.

3.3.1 Environment and Hardware Setup The evaluation was conducted in a typical office room, measuring approximately 3 meters by 3 meters. The room featured two ceiling-mounted diffused light sources and was furnished with tables and chairs, and was surrounded by orange walls, as shown in Figure 12.

To acquire ground truth data of the environment, we employed the TurtleBot3 Waffle Pi [35], a popular mobile robot platform, which is capable of autonomously navigation. We integrated a spectral sensor AS7265X [41], which measures 18 channels within the wavelength range of 410nm to 940nm, with the TurtleBot3 by attaching it to a Raspberry Pi 3B+ mounted on the robot. The spectral sensor was connected with an Arduino and oriented to face upwards, providing the capability to capture spectral readings of light in the environment. Data was sampled at a rate of 1 Hz. In total, we collected data from 176 different locations within the office room, creating a finely-grained spectral map with 14 channels as our groundtruth spectral map.

We also constructed a 3D model of the environment, using an iPhone 14 Pro Max, which features a LiDAR sensor and an RGB camera. In this process, a user holds the mobile phone and moves through the room, with the app providing real-time feedback on coverage. This visualization feature distinctly marks areas that have been successfully scanned and highlights those yet to be covered, guiding users to achieve comprehensive spatial data capture with simple human protocol. The scanning procedure took approximately 2 minutes to comprehensively record the entire office room. The spectrum of light sources and their locations within the office space were obtained from a building facility database/floormap. Material information for the 3D meshes within the environment was determined using the material estimation method of *LiDARSpectra* introduced in Section 2.3. In addition, we define coordinates for 176 locations sampled in the real environment by the Turtlebot3 described above.

LiDARSpectra produces light spectrum energy readings for 14 channels with wavelengths ranging from 410nm to 760nm. These

between light intensity and the inverse square of the distance shows that the light energy readings produced by *LiDARSpectra* follows the Inverse Square Law for light propagation closely.

Light Superposition. The superposition principle states that when two or more waves overlap in space, the total displacement is equal to the sum of displacements of individual waves. Since light has wave properties, the resulting light amplitude equals the algebraic sum of the amplitudes of individual waves [29]. We design a scene shown in Figure 9, where we place two light sources in an open environment[1]. The distance between the two lights is 50cm and the groundtruth light spectrometer is 35cm from the midpoint between them. Therefore, the distance between the sensor and the two lights is the same. The intensity ratio of light source 1 to light source 2 is 1 : 0.297.

We tested the two light sources by turning on each of them separately and together. Figure 10 shows the results produced by *LiDARSpectra* against groundtruth. The results are similar, which verifies *LiDARSpectra* performance in this scenario.

Reflectance. Light reflectence from objects in the scene is an important component of the light energy readings in different wavelengths (see Section 2.4.2). We construct a control scenario where the light source and groundtruth light spectrometer's positions are fixed but the colors of background fabric are different (see Figure 11 (top)). The location of the groundtruth sensor is behind the light bulb to maximize the impact of reflectance changes since, in this case, most light energy observed by the sensor is reflected light from the background fabric. Figure 11 (bottom) shows that the synthetic readings produced by *LiDARSpectra* in the groundtruth sensor's location are close to the sensor measurements.

---

[1]For light sources, we use Vintage Antique Edison Style Incandescent Clear Glass Light Lamp Bulb and a Bayonet 9W LED Globe Light Lamp Bulb.
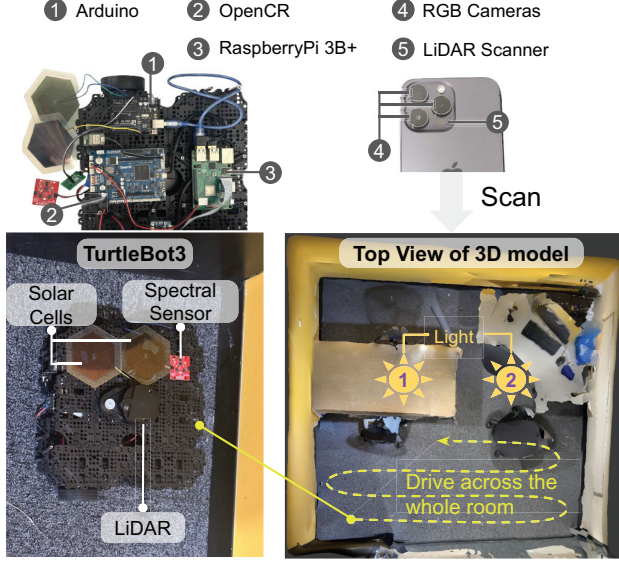
Figure 12: Hardware and environment for both spectral map and solar cell energy map data collections. Ground truth data was collected using a Turtlebot, while a 3D model was scanned and reconstructed using an iPhone in the same environment.

values are aligned with measurements produced by the spectral sensor AS7265x.

3.3.2 Evaluation Results Results obtained from the *LiDARSpectra* and groundtruth data were both normalized, scaling them to values between 0 and 1. The normalized results were plotted using interpolation techniques. Then we offer a series of visual representation, i.e., spectral maps, comprising 14 maps in total. Each map represents the intensity values of the 176 locations within the office room at one specific wavelength (see Figure 1). The ray tracing engine of our *LiDARSpectra* prototype also allows users to specify the maximum number of reflections that a light ray can take before it is terminated. We explore results for different settings of this parameter. Specifically, we study three scenarios: *low accuracy* scenario considers at most 2 reflections, *medium accuracy* considers 8 reflections, *high accuracy* considers 14 reflections and *ultra accuracy* considers 20 reflections. The material estimation component of our *LiDARSpectra* prototype was executed on an NVIDIA RTX 2080 Ti, while the ray tracing engine were conducted on a Mac Book Pro equipped with 16GB RAM M1 chip.

As shown in Figures 1a and 13d, the visualization of spectral map of real measurements and high-accuracy simulations reveals important insights. It is noteworthy that the irradiance distribution is clearly different for each wavelength. This observation highlights the richness of spectral data, which provides a depth of information beyond traditional intensity data. In addition, a comparison of the simulated spectral map with the real measured spectral map reveals a similarity, which reinforces the realism of our simulation model. For example, in the corresponding areas in the middle left and upper right corners, the map values consistently show lower intensities

Table 1: NRMSE and MAPE values with and without material estimation component of our generated spectral map in different simulation accuracies, and their ray tracing time.

	Ground Truth	Low	Medium	High	Ultra
NRMSE		0.437	0.313	0.283	0.284
MAPE		18.6%	14.4%	12.64%	12.74%
NRMSE w/o ME		0.565	0.515	0.537	0.533
MAPE w/o ME		48.8%	44.7%	45.2%	46.7%
Time (Minutes)		1	5	8	17

due to the table blocking the light from the ceiling (see Figure 1), thus, it matches human intuition and reflects the applicability of the model in the real world.

In order to quantitatively assess the difference between the groundtruth spectral distribution and the synthetic ones, we used the normalized root mean squared error (NRMSE) as an evaluation metric and Mean Absolute Percentage Error (MAPE), while the NRMSE indicates how far the synthetic spectrum fluctuates around the groundtruth [33], and the MAPE indicates average percentage error of synthetic spectrum relative to the groundtruth:

$$\text{NRMSE} = \frac{\sqrt{mean[(SI_{syn}(i) - SI_{real}(i))^2]}}{mean[SI_{real}(i)]} \tag{8}$$

$$\text{MAPE} = 100 \cdot \left| \frac{SI_{syn}(i) - SI_{real}(i)}{SI_{real}(i)} \right| \tag{9}$$

$SI_{syn}(i)$ represents the synthetic spectral irradiance produced by *LiDARSpectra* at wavelength i, while $SI_{real}(i)$ corresponds to the groundtruth spectral irradiance at the same wavelength i. We calculated the average NRMSE and MAPE for all locations and wavelengths, and the results are shown in Table 1. From the results we can observe that as the ray tracing fidelity (number of bounces) increases, the synthetic map's error reduces. For example, from low to high fidelity, the NRMSE decreases significantly, from 0.437 to 0.283. However, the improvement in fidelity comes at the cost of increased computation time, a challenge that could potentially be mitigated by more advanced hardware (e.g., more powerful GPUs). In addition, it is important to consider that the computation time is expected to increase as the 3D model size increases and complexity increases (i.e., meshed number increase). Increasing ray tracing fidelity beyond high accuracy shows diminishing returns, where the additional number of ambient bounces during ray tracing become counter-produtctive.

In conclusion, the results show that the system can generate accurate spectral data, with 0.283 NRMSE error compared to the groundtruth. Additionally, *LiDARSpectra* produces qualitatively accurate synthetic spectral map for realistic indoor environments, for example, areas with lower intensity in locations where the light source is obscured by an obstacle.

3.3.3 LiDARSpectra without Material Estimation The material estimation component in *LiDARSpectra* plays a important role in

the accuracy of synthetic spectral maps. To demonstrate the significance of this component, we conducted the same experiments as in the previous Section 3.3.2 without material estimation. Specifically, we assigned a default reflectance curve of white plastic, to all the 3D meshes.

Table 1 and Figure 13e show the results where material estimation was omitted. Specifically, NRMSE value increased significantly to 0.565, 0.515 and 0.537, respectively. Additionally, when material information is absent, the spectral map appears almost identical for all wavelengths, implying that little useful spectrum information can be extracted from the LSI data. These results suggest that the accuracy and fidelity of the synthetic spectral maps are degraded significantly if material information is not assigned to the 3D mesh. We have also visualized spectral maps in two additional non-controlled environments, as shown in Figure 13. These environments exhibit comparable performance to our initial findings. For example, at a wavelength of 460nm, both the real measurements and the synthetic results generated by *LiDARSpectra* reveal three high-intensity areas, showcasing a stark contrast to the maps generated without the material estimation component. Without the material estimation component, *LiDARSpectra* lacks the critical information needed to accurately calculate spectrum.

3.3.4   Impact of Default Material Selection   The selection of a default material in the absence of our material estimation component can affect the accuracy of synthetic spectral maps generated by *LiDARSpectra*. To quantify this impact, our evaluation was broadened to assess the performance of four additional materials—white wall, wooden cabinet, fully-reflective material, and non-reflective material—besides white plastic.

Table 2 shows that while the MAPE varies with the choice of default material, white plastic offers a surprisingly comparatively lower MAPE in our test environment. However, with ME activated, MAPE significantly outperformaning across all materials, reinforcing the ME component's crucial role in achieving precise spectral mapping.

Furthermore, with ME implemented, we set up threshold $T = 0.95$ in our evaluation, ensuring that at least 95% of surfaces within the environment are estimated. In this scenario, the lack of material information for the 5% of surfaces typically has minimal impact (See Table 2). This is because these surfaces are often obscured by objects or located in corners, areas that do not significantly influence the overall result.

The high-quality spectral map generated by *LiDARSpectra* can be utilised in many applications. In the next setcions, we will investigate the performance of *LiDARSpectra* in two real world application scenarios: LSI-based localization and indoor solar energy mapping.

3.4   LSI-based Indoor localization

3.4.1   Overall Localization Performance   Indoor localization has become a growing interest research area with a wide range of applications. An important approach in this field is Visible Light Positioning (VLP), an innovative technique for passive indoor localization using light information. In this section, we evaluate the performance of *LiDARSpectra* for the task of generating LSI fingerprints in a passive VLP system. Generating such fingerprints is an important calibration step that is time-consuming and has a critical impact on the VLP localization accuracy. Specifically, we compared the localization performance of the state-of-the-art spectral VLP system, *Iris* [17], for *LiDARSpectra*-generated and manually-collected fingerprints.

To evaluate the effectiveness of our spectral simulation system in the context of indoor localization, we conducted experiments in two distinct indoor environments: a typical large office setting and a apartment environment. In both environments, spectral sensors [41] were strategically placed to collect real-world spectral data. During the experiment, a participant entered the designated Area of Interest (AoI) and proceeded to move to predefined locations to collect the ground truth fingerprint. We have collected LSI fingerprints for 5 days, with each data collection process lasting approximately 3 hours for both environments.

We then re-created both environments using our *LiDARSpectra* prototype. In each case, we carefully scanned and reconstructed the 3D scenes and reproduced sensor positions to match the original real-world configuration. Their real and simulated spectral maps, without any human presence, are shown in Figure 13. In *LiDARSpectra*, we employed a 3D human model that matched body shape of the users. We simulated the users movement within the 3D environments to replicate the matching ground truth locations. We summarize the key parameters of two environments in Table 3.

We evaluate the localization accuracy using the Euclidean distance error metric [8] between the predicted location and ground truth. We utilized both real-world spectral data and synthetic map data produced by *LiDARSpectra* as training sets for the *Iris* classification network, reserving another set of real-world data for testing set. The experiments were conducted at three different *LiDARSpectra* ray tracing fidelity accuracy levels with and without Material Estimation (ME) component.

The results presented in Table 4 and Figure 14 demonstrate that *LiDARSpectra* can provide highly valuable fingerprints for the purposes of LSI-based localization. Moreover, our findings reveal that improvements in the simulated maps' fidelity, evidenced by a decrease in MAPE from 24.2% to 17.8% in office and from 25.0% to 19.1% in apartment, correlate with enhanced localization performance. Specifically, the median error in localization decreased correspondingly from 0.55m to 0.29m in office and 0.9m to 0.37m in apartment. Even using the low accuracy setting, the median localization error is sub-meter for both environments, i.e., $0.55m$ and $0.90m$ error for the office and the apartment, respectively. As expected, the localization performance increases with higher fidelity ray tracing settings.

In addition to achieving high levels of localization accuracy, *LiDARSpectra* offers substantial time-savings. For example, the traditional fingerprint collection required 10 hours in the office environment, while *LiDARSpectra* approach was able to reduce the process to just 10 minutes, representing a remarkable 60x improvement in efficiency. Similarly, in the smaller-sized apartment scenario, the fingerprint collection time is reduced from 4 hours for real spectral sensor fingerprint collection to approximately 5 minutes with *LiDARSpectra*, corresponding to a 50x increase in efficiency.

Table 2: MAPE values with and without Material Estimation component while using different materials

Material	White Plastic	White Wall	Wooden Cabinet	Fully Reflective Material	Non-Reflective Material
MAPE w/o ME	45.2%	62.3%	51.8%	69.7%	93.3%
MAPE with ME	12.7%	12.7%	12.6%	12.7%	12.8%

(a) Groundtruth large office spectra map.

(b) Synthetic large office spectral map.

(c) Synthetic large office spectral map

(d) Groundtruth apartment spectra map.

(e) Synthetic apartment spectra map.

(f) Synthetic apartment spectral map w/o ME.

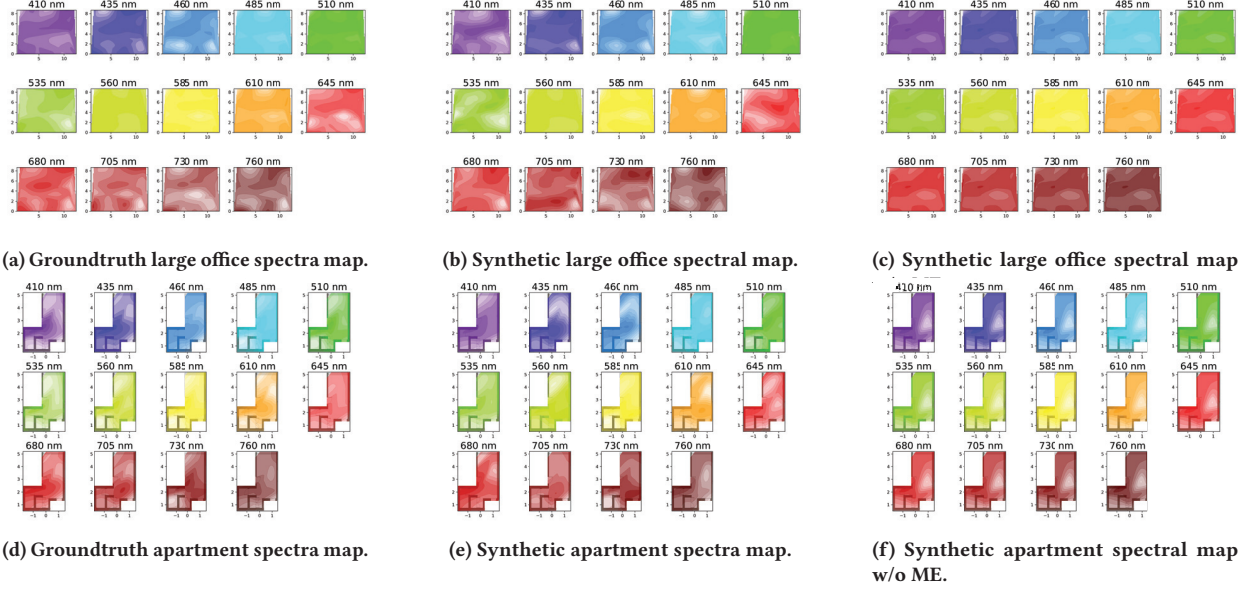**Figure 13: Sample spectral maps for two distinct indoor environments in the localization experiment: groudtruth vs. *LiDARSpectra* with and without material estimation.**

Table 3: Comparisons between office and apartment experimental environments.

Category	Office	Apartment
Light Sources	3 strip diffused light	11 LED Downlights
Sensor Number	27	17
Area Size	108 m^2	25 m^2
Collection Time	10 hours	4 hours 10 minutes
Scanning Time	10 minutes	5 minutes

Table 4: Median localization error in two environments using real fingerprints and *LiDARSpectra*-generated fingerprints.

Median error (m)	Environments	
	Office	Apartment
Iris [17]	0	0.06
Low	0.55	0.90
Medium	0.37	0.34
High	0.29	0.37

3.4.2 Localization Performance for Modified Environments Fingerprints are not static and are subject to change over time due to changes in the interior layout, such as the rearrangement of furniture, and in lighting sources. Over time, the environmental changes
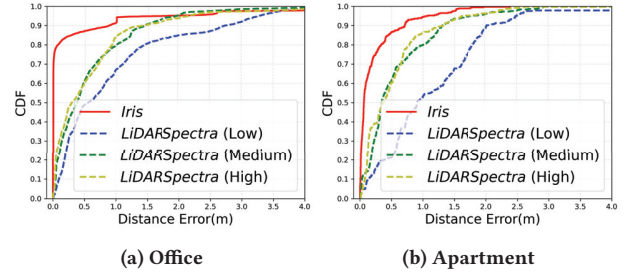

(a) Office

(b) Apartment

Figure 14: Localization error in two environments using real fingerprints and *LiDARSpectra*-Generated fingerprints.

will result in degraded localization performance and the operator will need to re-calibrate the VLI system by collecting new fingerprints.

We demonstrate this phenomenon in Figure 15. We collected LSI fingerprints in the same locations at two different times T1 and T2, separated by three months. Many locations in the figure show substantially different LSI fingerprints, underscoring the necessity for repeated fingerprint calibration.

LiDARSpectra provides an efficient tool to address the challenge of dynamic indoor environments with different layouts and simulating diverse lighting scenarios, including natural sunlight. With system's advanced ray tracing engine, it can meticulously replicate the behavior of different types of artificial lighting and natural sunlight
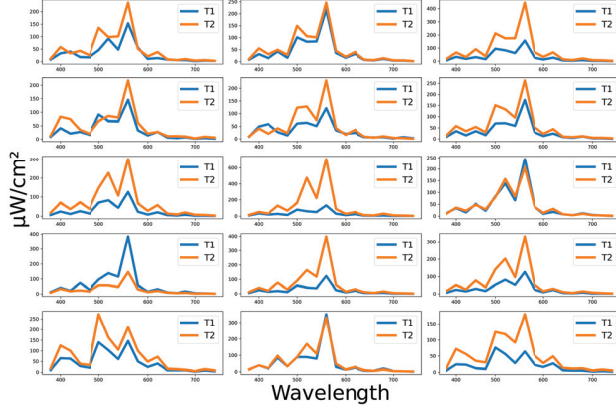
Figure 15: 15 sensors' raw readings in the same environment vary between measurements taken three months ago (T1) and three months later (T2).

Table 5: Localization error for unseen environment using measured LSI and synthetic LSI.

	Training Set	
	Measured LSI	Synthetic LSI
Median Error (m)	1.09	0.35
75th percentile error (m)	1.57	0.78
90th percentile error (m)	2.61	1.26

when given information about a specific light source. This method streamlines the re-calibration process necessitated by changes in the environment, utilizing a convenient and rapid 3D scanning technique achievable with a standard mobile phone.

We next provide a comparative evaluation of *Iris* performance in two scenarios: *Iris* trained on outdated LSI fingerprints collected at time T1 and *Iris* trained on *LiDARSpectra* LSI fingerprints based on a 3D environmental scan completed at time T2. In both scenarios, we test *Iris* performance on a test set spectral data collected at time T2.

We show the Cumulative Distribution Function (CDF) of the localization errors for both scenarios in Figure 16 and summarize the key results in Table 16. Clearly, localization performance of *Iris* can degrade significantly using outdated LSI fingerprints; for example, the 90th percentile error increased from $0.7m$ to $2.6m$. *LiDARSpectra* results demonstrate that the synthetic LSI fingerprints can produce substantially better localization performance.

In summary, we have demonstrated *LiDARSpectra*'s robust performance and adaptability in handling changes within indoor localization environments. The results show that the system is capable of providing reliable localization results, based on a fast 10-minute scanning period. *LiDARSpectra* offers a significant improvement compared to the 10-hour manual fingerprint collection process. Notably, *LiDARSpectra* is an important tool for maintaining high-accuracy localization in dynamic environments where furniture or light sources can be frequently re-arranged.
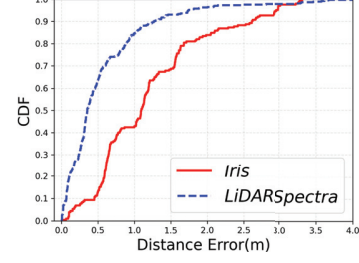

Figure 16: Localization error for unseen environment.

3.5 Indoor Solar Energy Mapping

Indoor solar energy harvesting through the use of solar cells is a compelling application of photovoltaic technology, offering the potential for generating clean, renewable energy within enclosed spaces [46]. Recent advancements in organic solar cell technology [37] have paved the way for the development of thin, lightweight, flexible, transparent, colored, and efficient solar cells tailored for indoor lighting conditions and decorations. Solar cells are now integrated into everyday IoT devices, including TV remote controllers [1], electronic window shade motors, and more. Understanding the feasibility of solar energy generation at specific indoor locations is invaluable for contemporary interior design, facilitating the optimal placement and design of solar-powered devices like digital photo frames and light switches throughout the space.

LiDARSpectra, capable of providing precise light intensities at specific wavelengths for any location, serves as an effective tool for estimating the photocurrent of a solar cell. This estimation is based on the cell's size and its absorption spectra, which characterizes its energy absorption across the entire light spectrum. In this section, we elucidate the theoretical foundation supporting this estimation and subsequently conduct an experiment to validate its accuracy.

The short-circuit current density (J_{sc}) is a crucial parameter in assessing the performance of a solar cell. It quantifies the maximum current a solar cell can deliver in the absence of any voltage applied, typically under standard test conditions. The mathematical expression for calculating J_{sc} involves the interaction between incident light and the semiconductor material of the solar cell [45]:

$$J_{sc} = \frac{q}{hc} \int_{\lambda_{min}}^{\lambda_{max}} EQE \cdot P_{in}(\lambda) \cdot \lambda \cdot d\lambda \tag{10}$$

Where q represents the elementary charge, c is the speed of light in free space, h denotes Planck's constant, λ_{min} and λ_{max} are the minimum and maximum wavelengths considered. EQE and $P_{in}(\lambda)$ is the ratio of photogenerated electrons collected to the number of incident photons and incident photons at wavelength (λ). This equation establishes a connection between the photon flux and the current density. The constant factor (q/hc) links the energy of an individual photon to its frequency, which, in turn, correlates to the number of photons reaching the solar cell. Therefore, given the spectral absorption rate and spectral response $a(\lambda)$, the incident spectrum $I(\lambda)$, and the surface area A of the solar cell, we can determine the current produced by the solar cell:

$$\text{Current} = A \cdot \int_{\lambda_{min}}^{\lambda_{max}} a(\lambda) \cdot I(\lambda) \cdot \lambda \cdot d\lambda \tag{11}$$

(a) Blue Solar Cell
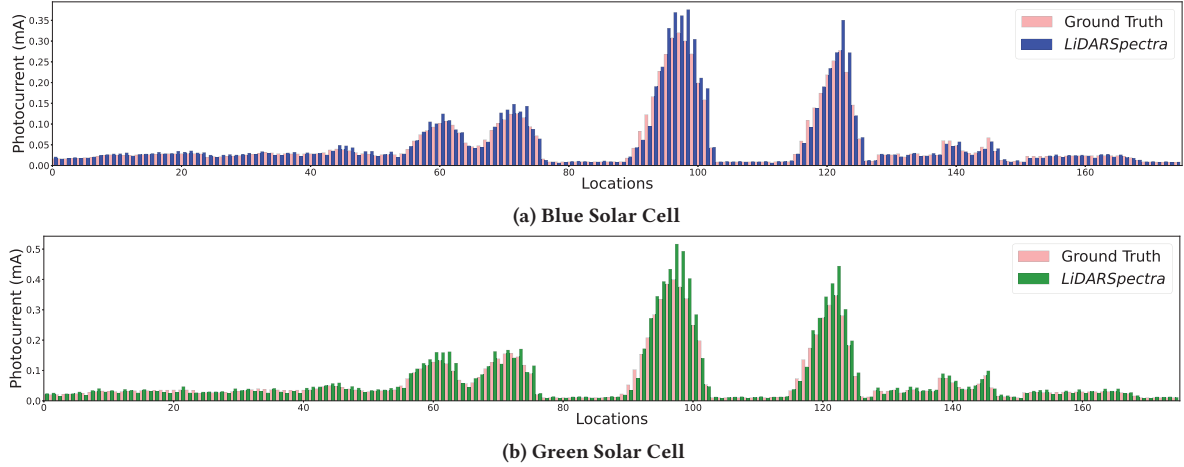

(b) Green Solar Cell

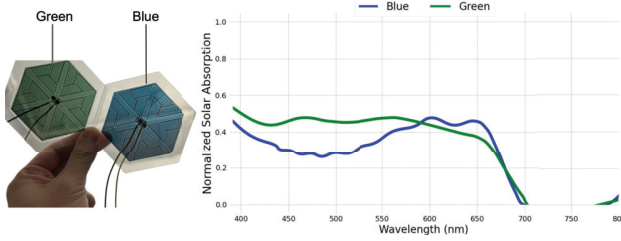**Figure 17: Solar energy comparison for all locations.**

Figure 18: Semi-transparent organic solar cells and their associated absorption rates employed in our experiment.

To assess the viability and efficacy of indoor solar energy mapping via *LiDARSpectra*, we carried out an experiment in a standard office room, as depicted in Figure 12. On a Turtlebot maneuvering throughout the room, we deployed a spectral sensor and two distinct solar cells, all linked to an Arduino analog-to-digital converter (ADC) for recording data on LSI and photocurrent. This allowed us to collect ground truth information regarding LSI and photocurrent. Additionally, we equipped the Turtlebot with a LiDAR to create a synthetic spectral map using *LiDARSpectra*.

The commercial semi-transparent organic solar cells [2] utilized in our experiments possess two distinct absorption rates, denoted as $a(\lambda)$, exemplified in Figure 18. These solar cells cover a surface area of 36 cm^2. Our spectral simulation system allowed us to access the incident spectrum information, $I(\lambda)$. Therefore, by utilizing Equation 11, we performed the conversion from spectral distribution to solar cell photocurrents.

Figure 17 presents a comparison between the simulated solar photocurrents based on the synthetic spectrum map produced by *LiDARSpectra* and the ground truth values across 176 locations where data was collected by the Turtlebot. The results demonstrate the remarkable accuracy of *LiDARSpectra* in mapping indoor solar energy for various solar cell designs. The minor discrepancies between the ground truth and estimated photocurrents are likely attributed to the use of plastic packaging material for the organic

---

[2]The solar cells and their associated absorption rate data were supplied by ASCA Technology https://www.asca.com/asca-technology/.

solar cells, which could affect the actual absorption rates compared to those measured in controlled laboratory conditions.

4 LIMITATION AND DISCUSSION

One of the challenges arises from the inherent limitations of the 2D material segmentation method [4] utilized in *LiDARSpectra*. While this approach offers a degree of accuracy, achieving a recognition rate of 73.1%, it does introduce the material misclassification and inaccuracies within our system. This shortcoming is primarily due to the inherent complexities of indoor environments, where materials like moss-covered bricks or unique-colored elements may not be adequately represented or classified in the database.

To enhance accuracy, we propose refining our approach by utilizing datasets focused on material reflectance for model training, aiming for better representation of real-world materials. Additionally, adopting advanced deep learning techniques could significantly improve recognition by leveraging the detailed spatial information provided by existing LiDAR data. These strategies are expected to reduce misclassification and enhance the system's performance.

The dependency on external light source data presents a limitation for *LiDARSpectra*. Recognizing this challenge, future iterations of the system will explore the development of enhanced estimation algorithms, which can be extended or complemented with a module dedicated to estimating light source positions and types based on the 3D geometry and RGB data captured, and the integration of user-input capabilities for light source characteristics.

In future work, we aim to broaden *LiDARSpectra*'s evaluation across diverse environments such as warehouses to solidify its adaptability and performance. Expanding these tests will further demonstrate its utility in varied applications, ensuring its robustness and efficacy in real-world scenarios.

5 RELATED WORK

Hyperspectral imaging is an advanced technology that goes beyond traditional RGB imaging to capture detailed spectral information in dozens of narrow bands across the electromagnetic spectrum. This powerful technique allows for the precise characterization of materials based on their unique spectral characteristics.

Table 6: Comparisons between *LiDARSpectra* and ALFA.

	Ours	ALFA [39]
Open-source	✓	✗
Add customized functions	✓	✗
Free	✓	✗
Main GUI operation software	Blender (Free)	Rhino (Subscription needed)
Light source wavelength range	Input by users	81 wavelengths (fixed)
Programming language	Python	C#
Operation systems	Mac, Linux, Windows	Windows

Hyperspectral cameras [3] are commonly employed for this purpose, capturing images that convey valuable material reflectance data. Our work extends the use of hyperspectral data, employing it alongside various other parameters, albeit with a unique emphasis. Unlike spectral cameras that capture spectral data in 2D from their field of view, *LiDARSpectra* utilizes LiDAR to obtain spectral information throughout a 3D environment, offering a holistic view of spatial spectral characteristics. While capable of 3D data collection, *LiDARSpectra* focuses on generating 2D spectral maps for practicality, ensuring detailed analysis without the limitations of direct line-of-sight restrictions faced by spectral cameras.

Spectral data is finding increasingly diverse applications across various fields. For example, *Iris* [17] and *SpectralLoc* [43] leverage spectral information to enhance the accuracy of indoor localization. Scientific studies have been conducted to use spatial hyperspectral imaging to detect and quantify changes in sensitive ecosystems, such as coral reefs [2]. Spectral data has also been used for predicting soil properties which is important in agricultural and environmental applications [28]. Spectral information has also been used to maximize solar cell conversion efficiency and optimize solar cell design [34].

As the applications of spectral data gain popularity, there is an increasing demand for a simulation tool capable of modeling complex 3D environments with detailed spectral data. Lark [18] introduced spectral light simulation by employing *n*-step ray tracing for individual wavelengths. Following a similar approach, ALFA [39] conducts spectral simulations using 81 wavelengths. However, both Lark and ALFA utilize Rhino [26] as the operational interface, which is proprietary and not freely available. In our work, we extend Blender [6], an open-source and freely accessible 3D modeling tool, to facilitate spectral simulations with full customization capabilities. This includes managing all spectral information, such as the reflectance spectra for individual surfaces within the 3D model, and the characteristics of light sources and their spectral profiles. A detailed comparison between our spectral extension of Blender and ALFA is presented in Table 6.

LiDAR stands for Light Detection and Ranging, a remote sensing technology that utilizes laser pulses to measure distances and produces accurate three-dimensional images of objects and the environment. LiDAR systems emit laser beams and measure the time it takes for the laser to bounce back after hitting an object, resulting in very detailed and accurate 3D maps. The technology has a wide range of applications, for example, navigation [5, 24, 38], 3D reconstruction [12, 20], object tracking [10], and recognition [31].

Automatic material recognition finds diverse applications, ranging from robotics and product search to image editing in interior design. Bell et al. [4] introduced an inventive pipeline that harnesses deep learning networks for material classification and segmentation in 2D images. In this paper, we expand upon their work by creating novel algorithms that associate material properties, including their reflectance spectra, with every surface within the 3D model generated using LiDAR. This process is essential for conducting 3D spectral ray tracing, a critical component in the creation of the indoor spectral map.

In wireless communications research, radio maps are instrumental for understanding radio signal propagation within an environment. These maps, developed through various methods, from empirical models [27, 47] to advanced simulations using ray tracing and generative AI [32, 48], primarily characterize signal strength, coverage, and interference with other wireless transmissions, aiding in wireless network planning and management. While radio maps focus on radio frequency signal propagation, our approach shifts the focus to spectral mapping, capturing material spectral properties and their interactions with incident light. This perspective provides crucial insights into spectral irradiance and energy distribution, particularly pertinent in applications like light-based indoor localization and energy management. In the following sections, we explore the importance and applications of this reflectance approach, providing fresh perspectives within the realm of visible light communications, sensing and energy harvesting.

6 CONCLUSION

In conclusion, this paper introduces *LiDARSpectra*, an innovative approach that holds the potential to revolutionize the way spectral data is acquired and utilized in various domains. *LiDARSpectra* streamlines the creation of spectral maps for indoor environments. It rapidly constructs a 3D model of the environment using LiDAR and RGB camera equipped on modern smartphones. LiDARSpectra employs a unique methodology to compute reflectance spectra for surfaces within the 3D model, enabling full-spectrum ray tracing to generate precise spectral maps within minutes. The results demonstrate *LiDARSpectra*'s effectiveness in producing up-to-date accurate spectral maps, reducing map generation time significantly. This capability is pivotal for applications requiring nuanced understanding of light's interaction with indoor environments such as indoor localization and solar-power IoT device energy planning, setting the stage for innovations in automated lighting control, enhanced occupant comfort, and energy-efficient building management.

Acknowledgments

References

[1] 2023. Original Samsung Smart TV Remote (Solar Cell Remote Control - BN59-01385B Genuine). https://remotecontrolwarehouse.com.au/products/.

[2] Touria Bajjouk, Pascal Mouquet, Michel Ropert, Jean-Pascal Quod, Ludovic Hoarau, Lionel Bigot, Nicolas Le Dantec, Christophe Delacourt, and Jacques Populus. 2019. Detection of changes in shallow coral reefs status: Towards a spatial approach using hyperspectral and multispectral data. *Ecological Indicators* 96 (2019), 174–191.

[3] Costas Balas, George Epitropou, Athanasios Tsapras, and Nikos Hadjinicolaou. 2016. A novel hyperspectral camera and analysis platform for the non-destructive material identification and mapping: An application in paintings by El Greco. In *2016 IEEE International Conference on Imaging Systems and Techniques (IST)*. IEEE, 211–215.

[4] Sean Bell, Paul Upchurch, Noah Snavely, and Kavita Bala. 2015. Material recognition in the wild with the materials in context database. In *Proceedings of the IEEE conference on computer vision and pattern recognition*. 3479–3487.

[5] Yi Cheng and Gong Ye Wang. 2018. Mobile robot navigation based on lidar. In *2018 Chinese control and decision conference (CCDC)*. IEEE, 1243–1246.

[6] Blender Online Community. 2018. *Blender - a 3D modelling and rendering package*. Blender Foundation, Stichting Blender Foundation, Amsterdam. http://www.blender.org

[7] Aleksandra Ćurčić, Aleksandar Kekovic, Dušan Ranđelović, and Ana Momcilovic-Petronijevic. 2019. Effects of color in interior design. *Zbornik radova Građevinskog fakulteta* 35 (2019), 867–877.

[8] Per-Erik Danielsson. 1980. Euclidean distance mapping. *Computer Graphics and image processing* 14, 3 (1980), 227–248.

[9] Lamp Spectral Power Distribution Database. 2022. LED EnergySmart BR30 Domestic. https://lspdd.org/app/en/lamps/2492.

[10] Iván del Pino, Víctor Vaquero, Beatrice Masini, Joan Sola, Francesc Moreno-Noguer, Alberto Sanfeliu, and Juan Andrade-Cetto. 2017. Low resolution lidar-based multi-object tracking for driving applications. In *Iberian Robotics conference*. Springer, 287–298.

[11] Dorukalp Durmus, Wenye Hu, and Wendy Davis. 2022. Lighting application efficacy: A framework for holistically measuring lighting use in buildings. *Frontiers in Built Environment* 8 (2022), 986961.

[12] Ahmed F Elaksher, James S Bethel, et al. 2002. Reconstructing 3d buildings from lidar data. *International Archives Of Photogrammetry Remote Sensing and Spatial Information Sciences* 34, 3/A (2002), 102–107.

[13] Mohamed Alyagoot Elgailani, Ahmed HH Al-Masoodi, Nohaidda Binti Sariff, and Nader Abdulrahman. 2021. Light dependent resistor sensor used for optimal power consumption for indoor lighting system. In *2021 2nd International Conference on Smart Computing and Electronic Enterprise (ICSCEE)*. IEEE, 237–242.

[14] James D. Foley, Andries van Dam, Steven K. Feiner, and John F. Hughes. 1996. *Computer Graphics: Principles and Practice* (2nd ed. ed.). Addison-Wesley, Reading, MA, USA.

[15] Andrew S Glassner. 1989. *An introduction to ray tracing*. Morgan Kaufmann.

[16] Bin Gu, Meiying He, Dongya Yang, Xuejie Yue, Fengxian Qiu, Tao Zhang, and Mingming Chen. 2020. Wearable Janus MnO2 hybrid membranes for thermal comfort management applications. *Applied Surface Science* 509 (2020), 145170.

[17] Jiawei Hu, Yanxiang Wang, Hong Jia, Wen Hu, Mahbub Hassan, Brano Kusy, Ashraf Uddin, and Moustafa Youssef. 2023. Iris: Passive Visible Light Positioning Using Light Spectral Information. *Proceedings of the ACM on Interactive, Mobile, Wearable and Ubiquitous Technologies* 7, 3 (2023), 1–27.

[18] Mehlika Inanici, Martin Brennan, and Edward Clark. 2015. Spectral daylighting simulations: Computing circadian light. In *Proceedings of BS2015: 14th Conference of International Building Performance Simulation Association, Hyderabad, India*. 1245–1252.

[19] J Alstan Jakubiec. 2016. Building a database of opaque materials for lighting simulation. In *PLEA 2016—Cities, Buildings, People: Towards Regenerative Environments, Proceedings of the 32nd International Conference on Passive and Low Energy Architecture*.

[20] Yoonseok Jwa, Gunho Sohn, and HB Kim. 2009. Automatic 3d powerline reconstruction using airborne lidar data. *Int. Arch. Photogramm. Remote Sens* 38, Part 3 (2009), W8.

[21] Pavlos Kalaitzoglou, Wim Van Ieperen, Jeremy Harbinson, Maarten Van der Meer, Stavros Martinakos, Kees Weerheim, Celine CS Nicole, and Leo FM Marcelis. 2019. Effects of continuous or end-of-day far-red light on tomato plant growth, morphology, light absorption, and fruit production. *Frontiers in plant science* 10 (2019), 322.

[22] Philipp Krähenbühl and Vladlen Koltun. 2013. Parameter learning and convergent inference for dense random fields. In *International Conference on Machine Learning*. PMLR, 513–521.

[23] Xinyu Ma, Sebastian Bader, and Bengt Oelmann. 2017. Characterization of indoor light conditions by light source classification. *IEEE Sensors Journal* 17, 12 (2017), 3884–3891.

[24] Flavio BP Malavazi, Remy Guyonneau, Jean-Baptiste Fasquel, Sebastien Lagrange, and Franck Mercier. 2018. LiDAR-only based navigation algorithm for an autonomous agricultural robot. *Computers and electronics in agriculture* 154 (2018), 71–79.

[25] Luzalen Marcos and Kristiina Valter Mai. 2020. Light spectra optimization in indoor plant growth for internet of things. In *2020 IEEE International IOT, Electronics and Mechatronics Conference (IEMTRONICS)*. IEEE, 1–6.

[26] Robert McNeel et al. 2018. *Rhinoceros 3D*. https://www.rhino3d.com/

[27] Piotr Mirowski, Tin Kam Ho, and Philip Whiting. 2014. Building optimal radio-frequency signal maps. In *2014 22nd International Conference on Pattern Recognition*. IEEE, 978–983.

[28] J Padarian, B Minasny, and AB McBratney. 2019. Using deep learning to predict soil properties from regional spectral data. *Geoderma Regional* 16 (2019), e00198.

[29] Robert L Pfleegor and Leonard Mandel. 1967. Interference of independent photon beams. *Physical Review* 159, 5 (1967), 1084.

[30] Charles R Qi, Hao Su, Kaichun Mo, and Leonidas J Guibas. 2017. Pointnet: Deep learning on point sets for 3d classification and segmentation. In *Proceedings of the IEEE conference on computer vision and pattern recognition*. 652–660.

[31] Baoxing Qin, Zhuang Jie Chong, Sooh Hong Soh, Tirthankar Bandyopadhyay, Marcelo H Ang, Emilio Frazzoli, and Daniela Rus. 2016. A spatial-temporal approach for moving object recognition with 2d lidar. In *Experimental Robotics: The 14th International Symposium on Experimental Robotics*. Springer, 807–820.

[32] Darwin Quezada-Gaibor, Joaquín Torres-Sospedra, Jari Nurmi, Yevgeni Koucheryavy, and Joaquín Huerta. 2022. SURIMI: Supervised radio map augmentation with deep learning and a generative adversarial network for fingerprint-based indoor positioning. In *2022 IEEE 12th International Conference on Indoor Positioning and Indoor Navigation (IPIN)*. IEEE, 1–8.

[33] Christoph F Reinhart and Marilyne Andersen. 2006. Development and validation of a Radiance model for a translucent panel. *Energy and buildings* 38, 7 (2006), 890–904.

[34] Jose M Ripalda, Jerónimo Buencuerpo, and Iván García. 2018. Solar cell designs by maximizing energy production based on machine learning clustering of spectral variations. *Nature Communications* 9, 1 (2018), 5126.

[35] ROBOTIS. 2023. TurtleBot3 Features. https://emanual.robotis.com/docs/en/platform/turtlebot3/features/.

[36] Alex Ryer, Ultraviolet Light, and Visible Light. 1997. Light measurement handbook. (1997).

[37] Felix Schubert and Daniel Spinner. 2016. Solar simulator spectrum and measurement uncertainties. *Energy Procedia* 92 (2016), 205–210.

[38] Shuyao Shi, Jiahe Cui, Zhehao Jiang, Zhenyu Yan, Guoliang Xing, Jianwei Niu, and Zhenchao Ouyang. 2022. VIPS: Real-time perception fusion for infrastructure-assisted autonomous driving. In *Proceedings of the 28th Annual International Conference on Mobile Computing And Networking*. 133–146.

[39] Solemma. 2017. AFLA: Adaptive Lighting for Alertness. https://www.solemma.com/alfa.

[40] Ryan Southall and Filip Biljecki. 2017. The VI-Suite: a set of environmental analysis tools with geospatial data applications. *Open Geospatial Data, Software and Standards* 2, 1 (2017), 1–13.

[41] SparkFun. 2022. SparkFun Triad Spectroscopy Sensor - AS7265x (Qwiic). https://www.sparkfun.com/products/15050.

[42] Christian Szegedy, Wei Liu, Yangqing Jia, Pierre Sermanet, Scott Reed, Dragomir Anguelov, Dumitru Erhan, Vincent Vanhoucke, and Andrew Rabinovich. 2015. Going deeper with convolutions. In *Proceedings of the IEEE conference on computer vision and pattern recognition*. 1–9.

[43] Yanxiang Wang, Jiawei Hu, Hong Jia, Wen Hu, Mahbub Hassan, Ashraf Uddin, Brano Kusy, and Moustafa Youssef. 2023. Spectral-Loc: Indoor Localization using Light Spectral Information. *Proceedings of the ACM on Interactive, Mobile, Wearable and Ubiquitous Technologies* 7, 1 (2023), 1–26.

[44] Gregory J Ward. 1994. The RADIANCE lighting simulation and rendering system. In *Proceedings of the 21st annual conference on Computer graphics and interactive techniques*. 459–4a72.

[45] Matthew Wright and Ashraf Uddin. 2012. Organic—inorganic hybrid solar cells: A comparative review. *Solar energy materials and solar cells* 107 (2012), 87–111.

[46] Lin Xie, Wei Song, Jinfeng Ge, Bencan Tang, Xiaoli Zhang, Tao Wu, and Ziyi Ge. 2021. Recent progress of organic photovoltaics for indoor energy harvesting. *Nano Energy* 82 (2021), 105770.

[47] Lun-Wu Yeh, Ming-Shiou Hsu, Yueh-Feng Lee, and Yu-Chee Tseng. 2009. Indoor localization: Automatically constructing today's radio map by iRobot and RFIDs. In *SENSORS, 2009 IEEE*. IEEE, 1463–1466.

[48] Songyang Zhang, Achintha Wijesinghe, and Zhi Ding. 2023. RME-GAN: A Learning Framework for Radio Map Estimation based on Conditional Generative Adversarial Network. *IEEE Internet of Things Journal* (2023).